




Distinct neutrino signatures of quark deconfinement in accretion-induced collapse of white dwarfs

Juno C. L. Chan ^{1,*} Harry Ho-Yin Ng ² and Patrick Chi-Kit Cheong ^{3,4,5}

¹*Center of Gravity, Niels Bohr Institute, Blegdamsvej 17, 2100 Copenhagen, Denmark*

²*Institut für Theoretische Physik, Goethe Universität,*

Max-von-Laue-Str. 1, 60438 Frankfurt am Main, Germany

³*Center for Nonlinear Studies, Los Alamos National Laboratory, Los Alamos, NM 87545, USA*

⁴*Department of Physics & Astronomy, University of New Hampshire, 9 Library Way, Durham NH 03824, USA*

⁵*Department of Physics, University of California, Berkeley, Berkeley, CA 94720, USA*

(Dated: March 11, 2025)

We present the first general relativistic neutrino-radiation simulations of accretion-induced collapse (AIC) of white dwarfs using hadron-quark matter equations of state with different onset densities of the first-order QCD phase transition (PT). The collapse forms a proto-neutron star that contracts due to neutrino cooling and softened mixed nuclear-quark matter, leading to a second bounce by deconfined quark matter and a stable proto-hybrid star. The distinct, detectable neutrino bursts and narrow AIC mass range could provide key constraints on hybrid star properties and PT onset density.

Introduction.— Carbon-oxygen white dwarfs (WDs) with masses of $\lesssim 1.2 M_\odot$ and high accretion rates are prone to carbon deflagration, leading to a Type Ia supernova that leaves no remnant [1–4]. In contrast, oxygen-neon WDs with masses of $\gtrsim 1.2 M_\odot$ and slower accretion rates can continue accreting material until they reach the Chandrasekhar limit around $1.44 M_\odot$ [5]. This triggers a gravitational collapse, followed by a core bounce, resulting in the formation of a proto-neutron star (PNS) remnant—a phenomenon known as accretion-induced collapse (AIC) [6].

AIC can occur via two main channels: mass transfer from a companion star to a WD in a binary system [7–9] or the binary WD merger [10–12]. The resulting super-Chandrasekhar WDs are often rapidly rotating [13–15] and magnetized [16–18] in both channels. Similar to core-collapse supernovae (CCSNe), AIC generates an intense electron neutrino (ν_e) burst after the core bounce associated with shockwave heating and the electron (e^-) capture processes on infalling matter. AIC has been suggested as a potential source of gamma-ray bursts, heavy r -process elements, kilonovae [19, 20], and gravitational waves (GWs) [21, 22].

It has been identified as a target for next-generation ground-based and space-based GW detectors [22–25]. The progenitors have also been associated with fast radio bursts [26, 27], further broadening their astrophysical significance.

On the other hand, active research of quantum chromodynamics (QCD) phase transition (PT) in compact stellar systems has primarily focused on CCSNe [28–34] and binary neutron star mergers [35–38]. Additionally, various types of PT that induce the collapse of isolated or accreting neutron star have been studied, including delayed onset of PT [39–41] and supersonic PT [42–44]. These studies highlight QCD PT in compact stellar systems as a promising source of multi-messenger signals,

EOS	ρ_{onset} [$10^{14} \text{ g cm}^{-3}$]	M_{max} [M_\odot]	M_{onset} [M_\odot]
RDF-1.9	4.6	2.16	0.81
RDF-1.2	7.3	2.15	1.37
RDF-1.5	8.2	2.03	1.46
RDF-1.1	8.8	2.13	1.55

TABLE I. The hybrid EOSs employed in our simulations with the same initial gravitational mass of the progenitor of $M = 1.51 M_\odot$. ρ_{onset} and M_{onset} denote the onset density and onset gravitational mass of the PT starting to reach the mixed phase, where these three quantities are defined under $T = 0 \text{ MeV}$ and $Y_p = 0.3$ [28]. The maximum gravitational mass of the non-rotating model is denoted as M_{max} for each EOS.

facilitating hybrid star formation and constraining the hadron-quark matter equation of state (EOS). Therefore, it is reasonable to ask the possibilities of PT in AIC systems, and the associated signatures.

In this Letter, we present the first seconds-long general relativistic neutrino-radiation simulations of the AIC systems that employ realistic hadron-quark hybrid EOSs to explore the possibilities of the occurrence of first-order PT, the existence of deconfined quark matter and the properties of hybrid stars.

Numerical methods and setups.— We use a set of hadron-quark hybrid EOSs, known as relativistic density functional (RDF) EOSs, where both quark and hadron matter are described within the RDF formalism [45]. A first-order PT connects the hadronic phase to the stiffer deconfined quark phase, forming mixed nuclear-quark matter. The RDF EOSs incorporate varying onset densities and latent heats, with deconfined quark matter modeled using a string-flip approach. These EOSs are consistent with astrophysical constraints, including precise high-mass neutron star measurements [46] and recent NICER results [47]. These EOSs have been recently utilized in astrophysical simulations [31, 32, 34, 48].

EOS	t_{mixed} [s]	$\rho_{\text{mixed,c}}$ [10^{14} g cm^{-3}]	$T_{\text{mixed,c}}$ [MeV]	M_{mixed}^b [M_{\odot}]	t_{Q} [s]	M_{Q}^b [M_{\odot}]	M_{MM}^b [M_{\odot}]	M_{PHS}^b [M_{\odot}]	r_{Q} [km]	r_{MM} [km]	r_{PHS} [km]	\mathcal{L}_{ν_e}	$\mathcal{L}_{\bar{\nu}_e}$ [10^{51} erg^{-1}]	\mathcal{L}_{ν_x}	$\langle \epsilon_{\nu_e} \rangle$	$\langle \epsilon_{\bar{\nu}_e} \rangle$	$\langle \epsilon_{\nu_x} \rangle$
RDF-1.9	0.58	4.1	17.8	1.53364	1.11	1.082	0.15	1.524	5.93	6.66	12.7	148	837	501	28.8	59.6	104.7
RDF-1.2	1.56	5.3	23.4	1.53459	2.91	0.92	0.23	1.531	5.42	6.34	10.7	194	412	187	44	50.5	91.8
RDF-1.5	3.06	5.94	26.6	1.53467	4.27	0.875	0.19	1.533	4.92	5.61	9.64	49.8	65.2	21.2	31.8	34.1	46.9
RDF-1.1	3.33	6.03	27.5	1.53469	6.44	0.288	0.61	1.533	4.14	5.29	9.82	6.59	16	8.03	20.8	24.3	24.2

TABLE II. Various quantities extracted at the moment of first reaching the mixed nuclear-quark phase (columns in the left part) and 300 ms after the first entry into the deconfined quark phase (columns in the right part) in our simulations, using different RDF EOS. t_{mixed} , $\rho_{\text{mixed,c}}$, $T_{\text{mixed,c}}$ and M_{mixed}^b denote the the time after the first core bounce at $t = t_b$, central density, central temperature and the enclosed baryon mass of the PNS for the system first reaching the mixed nuclear-quark phase. t_{Q} is the time first reaching the deconfined quark phase with respect to t_b . Baryon mass (radius) of the quark core, the mixed-phase mantle (MM) and the new-born proto-hybrid star (PHS), are expressed as M_{Q}^b (r_{Q}), M_{MM}^b (r_{MM}) and M_{PHS}^b (r_{PHS}). The peak values of neutrino luminosity and averaged energy of the second neutrino burst is evaluated at $r = 500$ km and represented as \mathcal{L}_{ν_l} and $\langle \epsilon_{\nu_l} \rangle$, respectively for electron neutrino ν_e , electron antineutrino $\bar{\nu}_e$ and a collective species describing heavy lepton neutrinos and their antineutrinos as ν_x . Note that the PNS or PHS are defined as the regions of $\rho > 10^{11}$ g cm $^{-3}$.

All progenitors are spherically symmetric, non-rotating, with a gravitational mass of $1.51 M_{\odot}$, generated via RNS [49]. To explore the impact of PT onset density, we use the RDF EOSs listed in Table I. Our simulations employ the general relativistic neutrino-radiation hydrodynamics code `Gmumu` [50–54], which solves Einstein’s field equations under the conformal flatness condition [50, 55–57].

We adopt the energy-integrated two-moment neutrino transport scheme [58, 59], and the implicit-explicit Runge-Kutta method IMEX-SSP2(2,2,2) [60] for time integration. For the neutrino microphysics, we employ the neutrino library `WeakHub` [54] and consider the conventional set of weak interactions defined in Ref. [54] but excluding inelastic neutrino-electron scattering. Neutrino opacities are tabulated after averaging in energy space (see Ref. [59]), where the neutrino energy is logarithmically discretised into 20 bins within the range [0.1, 400] MeV. The emissivities are recalculated on-the-fly using Kirchhoff’s law.

Given the uncertainties in the e^- capture rates on heavy nuclei [61], during collapse of the progenitor of AIC before core bounce (defined as when the matter specific entropy $s \geq 3$ kb/baryon in the core region), We apply an effective deleptonization scheme [62] to mimic the proton fraction Y_p profile a function of rest-mass density ρ , which is widely used in AIC simulations [19, 21, 22].

The computational domain extends to $[0, 3 \times 10^3]$ km at the outer boundary, with a resolution $N_r = 128$. The finest grid size at the center of the star is 45.8 m.

Results.— When the progenitor collapses to nuclear density, ρ_{sat} , hadronic matter stiffens, halting the collapse and triggering a core bounce and an outward shock at $t = t_b$. This produces a ν_e burst with $\mathcal{L}_{\nu_e} \sim 10^{53}$ ergs $^{-1}$ over ~ 10 ms [19, 22] and detailed in End-Matter (EM).

The PNS gradually loses energy through weaker neutrino emissions across all species, maintaining $\mathcal{L}_{\nu_l} \sim 10^{51}$ ergs $^{-1}$ for several seconds. This sustained emission depletes thermal energy and pressure, leading to gradual

contraction via Kelvin-Helmholtz cooling, which slowly increases ρ_c and T_c .

The contraction accelerates upon reaching the onset of a first-order PT, forming mixed nuclear-quark phase matter, i.e. quark fraction $Y_q > 0$, which softens the EOS. The left columns of Table II show the time t_{mixed} , central density $\rho_{\text{mixed,c}}$, central temperature $T_{\text{mixed,c}}$ and the enclosed baryonic mass of the PNS M_{mixed}^b when the system first reaches the mixed phase with $Y_q > 0$, for all models. M_{mixed}^b differs by under 0.07% across models, indicating that the accretion phase is effectively ended and a steady PNS has formed at this point (see discussion in Fig. 2). Due to the high T_c and low Y_p at the PNS core, the modified onset density $\rho_{\text{mixed,c}}$ is lower than ρ_{onset} in Table I, which is defined under $T = 0$ MeV and $Y_p = 0.3$ [45]. For example, $\rho_{\text{mixed,c}}$ is 30% (10%) lower than ρ_{onset} in model RDF-1.1 (RDF-1.9), corresponding to $T_{\text{mixed,c}}$ of 27.5 MeV (17.8 MeV) at $t = t_{\text{mixed}}$. After $t = t_{\text{mixed}}$, $T_{\text{mixed,c}}$ is further reduced by the latent heat absorption, leading to an increase in $Y_{q,c}$. As contraction accelerates at the first-order PT onset, mixed nuclear-quark matter forms ($Y_q > 0$), softening the EOS.

Figure 1 illustrates the evolution of central density ρ_c (solid) and quark fraction $Y_{q,c}$ (dotted) through three phases: the mixed phase ($Y_{q,c} < 1$), the onset of deconfined quark matter ($Y_{q,c} = 1$) at t_{Q} (first entry into the deconfined quark phase relative to t_b , see Table II), and the quasi-stable proto-hybrid star (PHS) phase.

In the first phase, increasing Y_q accelerates collapse as the EOS softens. A greater fraction of mixed-phase matter leads to faster collapse, meaning higher $\rho_{\text{mixed,c}}$ results in a longer time to reach t_{mixed} . As the core approaches the stiffer deconfined quark phase at $t \approx t_{\text{Q}}$, collapse within 0.5 ms. For all RDF EOSs, the system’s small baryonic mass ($\sim 1.53 M_{\odot}$) and the stiffness of deconfined quark matter prevent direct black hole formation. Instead, the stiff quark core halts the infall of mixed-phase material, generating a second outward-propagating shock. This shock, at high density and

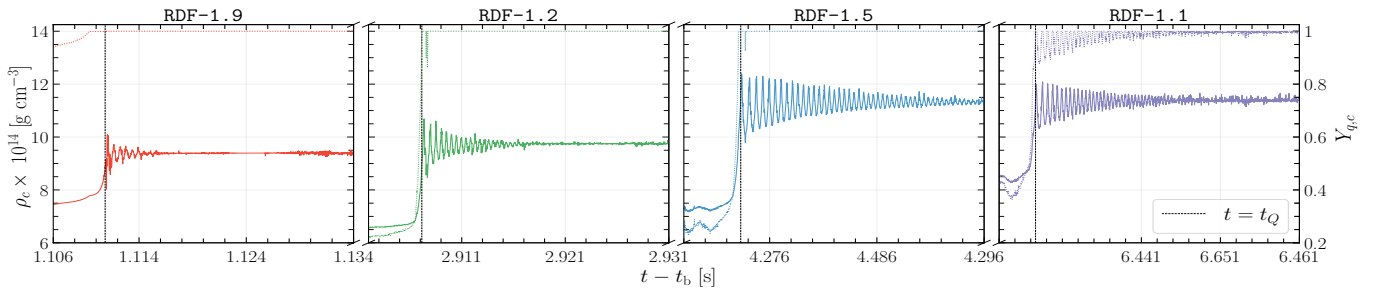


FIG. 1. Time evolution of the central density ρ_c (solid lines) and central quark fraction $Y_{q,c}$ (dotted lines) after the first core bounce for all models. The second bounce for $t - t_b < 23$ ms are shown. Dashed lines correspond to the time at $t = t_Q$.

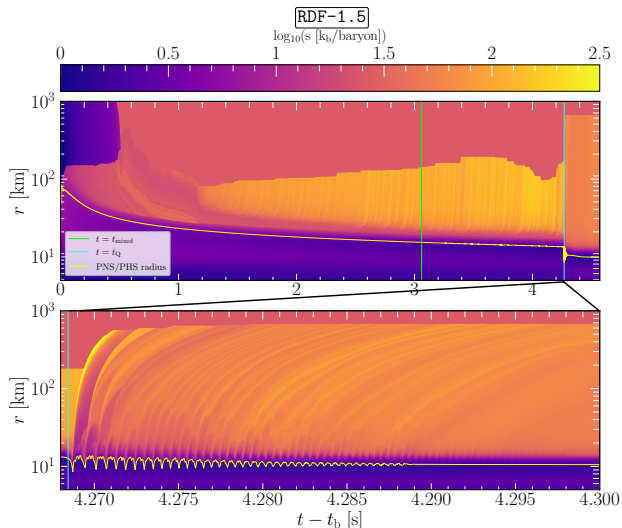


FIG. 2. Specific entropy s profile of the model with RDF-1.5 EOS. *Top panel:* From $t = t_b$ to 300 ms after t_Q . *Bottom panel:* From $t = t_Q$ to 32 ms after t_Q . The vertical lines indicate time moments of $t = t_{\text{mixed}}$ (lime) and $t = t_Q$ (cyan). The yellow solid line represents the radius of PNS or PHS.

temperature, converts infalling hadronic matter into the mixed phase and accelerates as it reaches the lower-density hadronic envelope near the PNS surface.

The second shock energizes the hadronic envelope, enhances e^+ captures, and produces a second neutrino burst (see detailed discussion on the second burst later).

A quasi-stable PHS forms in each case, comprising a quark core, a mixed-phase mantle, and a residual hadronic envelope with baryonic masses M_Q^b , M_{mixed}^b , and M_{PHS}^b , respectively, as listed in Table II (right columns). The over-compression of the quark core before the second bounce, combined with dynamic changes in quark and mixed-phase matter, induces strong perturbations in the newborn PHS, leading to rapid oscillations that damp out within ~ 23 ms in Fig. 1.

To examine the dynamics around the second bounce, we focus on the RDF-1.5 EOS case. The upper panel of Fig. 2 shows the specific entropy s evolution from

$t - t_b$ to 300 ms after t_Q . The first core bounce generates a shock that expands to ~ 90 km within 5 ms. By $t - t_b \sim 10$ –100 ms, the shock loses energy, stalls at ~ 100 km, and forms an accreting envelope with $s \sim 7$ –15 k_b /baryon. This agrees quantitatively with early post-bounce evolution in non-rotating models [20, 22].

After core bounce, the PNS mass increases from $0.92M_\odot$ at $t = t_b$ to $1.534 M_\odot$ by $t - t_b \sim 600$ ms due to the accretion of infalling shocked matter and material from the outer envelope.

As accretion diminishes, the system reaches a steady state with a baryonic mass of $1.535 M_\odot$ at $t - t_b \approx 1.2$ s. Despite entering the mixed phase, the PNS continues to contract (see yellow line in Fig. 2), reinforcing that neutrino cooling and mixed-phase matter soften the EOS. Additionally, the high-entropy matter ($s \sim 25$ –50 k_b /baryon) observed at 30–100 km after $t - t_b \sim 1$ s arises from interactions between the accretion envelope and fallback of ejected matter from the first shock.

Immediately after $t = t_Q$, the newly formed PHS core undergoes a second bounce, generating a shock that propagates to ~ 500 km in 2.4 ms at $\sim 0.5 c$ (see Fig. 2, lower panel). As it pushes against dense matter beyond the accretion envelope, heating it to $\sim 50 k_b$ /baryon, it loses energy and stalls at ~ 500 km. Before stalling, PHS oscillations produce multiple weaker shocks ($\sim 0.25 c$) that continue pushing matter outward, expanding the envelope to ~ 600 km within 4 ms. Since the accreting envelope in AIC systems is only $\sim 0.1\%$ of the total mass, the second shock loses less energy and propagates beyond the first shock stall (~ 100 km), reaching at least 500 km (RDF-1.1) and up to 1500 km (RDF-1.9). Following the second bounce, the PHS rapidly contracts, with the radius shrinking by $\sim 20\%$ at 50 ms after t_Q and continuing to contract gradually. This shock, propagating through the low-proton-fraction region, generates a second neutrino burst.

Figure 3 presents the neutrino luminosity, \mathcal{L}_{ν_i} , and average energy, $\langle \epsilon_{\nu_i} \rangle$, for all species during the second millisecond neutrino burst in the RDF-1.5 model. The burst, with luminosities on the order of 10^{52} ergs $^{-1}$, is triggered by the second shock as it propagates through the PHS

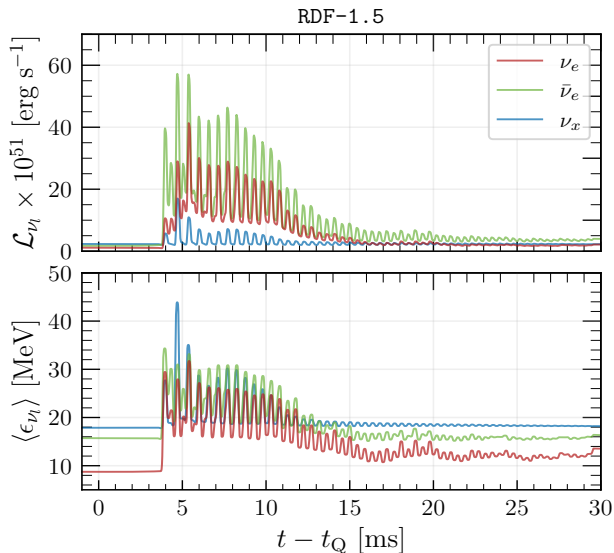


FIG. 3. Time evolution of neutrino luminosity \mathcal{L}_{ν_i} and average energy $\langle \epsilon_{\nu_i} \rangle$ of the second neutrino burst formed in the case with RDF-1.5 EOS for ν_e (red), $\bar{\nu}_e$ (green) and ν_x (blue), respectively.

neutrinospheres and is observed around 4 ms after t_Q .

At the onset of the burst, neutrino luminosities and average energies for all species reach a peak, as summarized in Table II (right columns). The burst is dominated by $\bar{\nu}_e$ due to positron (e^+) capture in the low-proton-fraction cavity during shock propagation. Also, the stronger second shock produces neutrinos with higher average energy across all species compared to the first shock. See EM for a comparison of the first and second bursts.

These quantities then oscillate for ~ 30 ms, corresponding to the oscillation and damping of the PHS following the second bounce (Fig. 1). This oscillatory behavior in the second burst, lasting 5–30ms, is consistently observed across all models, and is also indicated in the CCSNe simulations in [33, 63].

The second neutrino burst not only confirms a strong first-order PT and PHS formation but also provides a key observational probe. The time interval between the two bursts, approximately t_Q , constrains the onset density and PT properties. As shown in Table II, small variations in $\rho_{\text{mixed,c}}$ across different EOSs lead to significant differences in t_Q , often exceeding a second.

Figure 4 presents empirical relations between t_Q (top panel), total neutrino luminosity \mathcal{L}_{tot} (middle panel), and $\langle \epsilon_{\bar{\nu}_e} \rangle$ (bottom panel) as functions of $\rho_{\text{mixed,c}}$. The top panel shows that t_Q increases significantly with $\rho_{\text{mixed,c}}$, unlike QCD PT simulations in CCSNe, where t_Q varies linearly with ρ_{onset} on shorter timescales of ~ 0.1 s [28]. This discrepancy arises because, in AIC systems, the accreting and infalling mass is negligible compared to CCSNe, resulting in slower neutrino cooling and mixed-

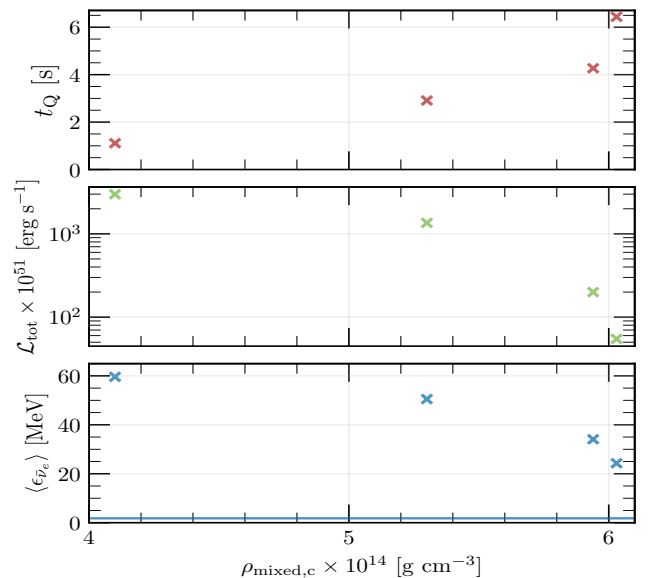


FIG. 4. Empirical relations of t_Q , the total neutrino luminosity \mathcal{L}_{tot} and $\langle \epsilon_{\bar{\nu}_e} \rangle$ as functions of $\rho_{\text{mixed,c}}$. The blue horizontal line indicates the detectable energy range for water Cherenkov detectors via inverse beta decay [64–67].

phase accumulation, and thus a much longer t_Q .

For these reasons, new relationships between neutrino observables and $\rho_{\text{mixed,c}}$ (middle and bottom panels of Fig. 4) emerge. These empirical relations directly link detectable neutrino signals to $\rho_{\text{mixed,c}}$ in AIC systems, offering four distinct advantages for constraining the onset density of the first-order PT. Notably, these relations are unique to AIC and do not appear in CCSNe simulations using the same RDF EOS family [28].

Given the 1.8 MeV inverse beta decay energy threshold [64–67], the $\bar{\nu}_e$ signatures are detectable via inverse beta decay in water Cherenkov detectors [64–67].

Due to the advantageous second-long time separation between the two neutrino bursts in AIC systems, along with their less massive accretion envelopes and a narrower total mass range of $1.44\text{--}2.56 M_\odot$ [68] (in contrast to the broader $8\text{--}100 M_\odot$ range in CCSNe [69]), exploring first-order PT in AIC scenarios results in smaller uncertainties, particularly in neutrino observables, than PT in CCSNe. This could enable exceptionally tight constraints on PT and QCD matter properties from the detection of a single galactic AIC event.

Conclusion.— We present the first seconds-long general relativistic neutrino-radiation simulations of AIC with realistic hadron-quark hybrid EOSs, evolving the collapse of $1.51 M_\odot$ super-Chandrasekhar WDs. A first-order PT triggers the formation of a quasi-stable PHS with a deconfined quark core and a distinct second neutrino burst.

Following core bounce, the PNS undergoes slow contraction due to neutrino cooling, with the appearance of mixed nuclear-quark matter further softening the core

and slightly accelerating collapse. The transition to a stiff deconfined quark core halts the collapse, generating a second shock breakout and a $\bar{\nu}_e$ -dominated burst with higher average neutrino energy across all species compared to the first burst. In all cases, a stable PHS forms, consisting of a deconfined quark core, a mixed-phase mantle, and an outer hadronic envelope.

AIC provides a promising avenue for constraining PT thresholds and hybrid EOS properties. Unlike CCSNe, its narrower mass range and a less massive accreting envelope, making them ideal for studying QCD PT and PHS properties through observational signatures. We establish an empirical relation between PT onset density and neutrino observables, particularly the time delay between the two bursts as a function of the PT onset density.

Our results suggest that a single galactic AIC neutrino detection could impose precise constraints on PT thresholds, hybrid EOS properties, and the existence of HSs. These findings may also impact our understanding of GW emission, gamma-ray bursts, and r -process nucleosynthesis [70] in AIC systems. Future work will incorporate multi-dimensional effects, including rotation, accretion instabilities [20], more advanced microphysics [71–73], and the inclusion of magnetic fields [19].

Acknowledgement.— The authors thank Liang Dai, Christian Ecker, Jose Maria Ezquiaga, Tobias Fischer, JJ Hermes, Jin-Liang Jiang, Pablo Martínez-Miravé and Luciano Rezzolla for the useful discussion. J.C.L.C. acknowledges support from the Villum Investigator program supported by the VILLUM Foundation (grant no. VIL37766 and no. VIL53101) and the D NRF Chair program (grant no. D NRF162) by the Danish National Research Foundation. H.H.Y.N. is supported by the European Research Council Advanced Grant “JETSET: Launching, propagation and emission of relativistic jets from binary mergers and across mass scales” (grant No. 884631). P.C.-K.C. gratefully acknowledges support from NSF Grant PHY-2020275 (Network for Neutrinos, Nuclear Astrophysics, and Symmetries (N3AS)). The Tycho supercomputer hosted at the SCIENCE HPC center at the University of Copenhagen was used for supporting this work.

* chun.lung.chan@nbi.ku.dk

- [1] S. C. Yoon, P. Podsiadlowski, and S. Rosswog, Remnant evolution after a carbon-oxygen white dwarf merger, *MNRAS* **380**, 933 (2007), [arXiv:0704.0297 \[astro-ph\]](https://arxiv.org/abs/0704.0297).
- [2] K. J. Shen and L. Bildsten, The Effect of Composition on Nova Ignitions, *ApJ* **692**, 324 (2009), [arXiv:0805.2160 \[astro-ph\]](https://arxiv.org/abs/0805.2160).
- [3] K. J. Shen, I. Idan, and L. Bildsten, Helium Core White Dwarfs in Cataclysmic Variables, *ApJ* **705**, 693 (2009), [arXiv:0906.3767 \[astro-ph.HE\]](https://arxiv.org/abs/0906.3767).
- [4] K. Moore, D. M. Townsley, and L. Bildsten, The Effects of Curvature and Expansion on Helium Detonations on White Dwarf Surfaces, *ApJ* **776**, 97 (2013), [arXiv:1308.4193 \[astro-ph.SR\]](https://arxiv.org/abs/1308.4193).
- [5] S. Chandrasekhar, The Maximum Mass of Ideal White Dwarfs, *ApJ* **74**, 81 (1931).
- [6] K. Nomoto and Y. Kondo, Conditions for Accretion-induced Collapse of White Dwarfs, *ApJ* **367**, L19 (1991).
- [7] K. Nomoto and Y. Kondo, Conditions for accretion-induced collapse of white dwarfs, *Astrophysical Journal*, Part 2-Letters (ISSN 0004-637X), vol. 367, Jan. 20, 1991, p. L19-L22. **367**, L19 (1991).
- [8] T. M. Tauris, D. Sanyal, S.-C. Yoon, and N. Langer, Evolution towards and beyond accretion-induced collapse of massive white dwarfs and formation of millisecond pulsars, *Astron. Astrophys.* **558**, A39 (2013), [arXiv:1308.4887 \[astro-ph.SR\]](https://arxiv.org/abs/1308.4887).
- [9] B. Wang, The single-degenerate model for the progenitors of accretion-induced collapse events, *Mon. Not. Roy. Astron. Soc.* **481**, 439 (2018), [arXiv:1808.05992 \[astro-ph.SR\]](https://arxiv.org/abs/1808.05992).
- [10] A. J. Ruiter, Type Ia Supernova Sub-classes and Progenitor Origin, *IAU Symp.* **357**, 1 (2019), [arXiv:2001.02947 \[astro-ph.SR\]](https://arxiv.org/abs/2001.02947).
- [11] D. Liu and B. Wang, The formation of single neutron stars from double white-dwarf mergers via accretion-induced collapse, *Mon. Not. Roy. Astron. Soc.* **494**, 3422 (2020), [arXiv:2004.03157 \[astro-ph.SR\]](https://arxiv.org/abs/2004.03157).
- [12] B. Wang and D. Liu, The formation of neutron star systems through accretion-induced collapse in white-dwarf binaries, *Res. Astron. Astrophys.* **20**, 135 (2020), [arXiv:2005.01880 \[astro-ph.SR\]](https://arxiv.org/abs/2005.01880).
- [13] L. Piersanti, S. Gagliardi, I. Iben, Jr., and A. Tornambe, Carbon - oxygen white dwarfs accreting CO-rich matter I: A Comparison between rotating and non-rotating models, *Astrophys. J.* **583**, 885 (2003), [arXiv:astro-ph/0210624](https://arxiv.org/abs/astro-ph/0210624).
- [14] T. Uenishi, K. Nomoto, and I. Hachisu, Evolution of rotating accreting white dwarfs and the diversity of type Ia supernovae, *Astrophys. J.* **595**, 1094 (2003), [arXiv:astro-ph/0309433](https://arxiv.org/abs/astro-ph/0309433).
- [15] H. Saio and K. Nomoto, Off - center carbon ignition in rapidly rotating, accreting carbon - oxygen white dwarfs, *Astrophys. J.* **615**, 444 (2004), [arXiv:astro-ph/0401141](https://arxiv.org/abs/astro-ph/0401141).
- [16] L. Ferrario, D. de Martino, and B. T. Gänsicke, Magnetic White Dwarfs, *Space Sci. Rev.* **191**, 111 (2015), [arXiv:1504.08072 \[astro-ph.SR\]](https://arxiv.org/abs/1504.08072).
- [17] A. Kawka, Clues to the origin and properties of magnetic white dwarfs, *IAU Symposium* **357**, 60 (2020), [arXiv:2001.10672 \[astro-ph.SR\]](https://arxiv.org/abs/2001.10672).
- [18] L. Ferrario, D. Wickramasinghe, and A. Kawka, Magnetic fields in isolated and interacting white dwarfs, *Advances in Space Research* **66**, 1025 (2020), [arXiv:2001.10147 \[astro-ph.SR\]](https://arxiv.org/abs/2001.10147).
- [19] P. C.-K. Cheong, T. Pitik, L. F. L. Micchi, and D. Radice, Gamma-ray bursts and kilonovae from the accretion-induced collapse of white dwarfs, (2024), [arXiv:2410.10938 \[astro-ph.HE\]](https://arxiv.org/abs/2410.10938).
- [20] E. Batziou, R. Glas, H. T. Janka, J. Ehring, E. Abdikamalov, and O. Just, Nucleosynthesis Conditions in Outflows of White Dwarfs Collapsing to Neutron Stars, (2024), [arXiv:2412.02756 \[astro-ph.HE\]](https://arxiv.org/abs/2412.02756).
- [21] E. B. Abdikamalov, C. D. Ott, L. Rezzolla, L. Dessart, H. Dommelmeier, A. Marek, and H. T. Janka, Axisymmetric General Relativistic Simulations of the Accretion-

- Induced Collapse of White Dwarfs, *Phys. Rev. D* **81**, 044012 (2010), [arXiv:0910.2703 \[astro-ph.HE\]](#).
- [22] L. F. Longo Micchi, D. Radice, and C. Chirenti, Multimessenger emission from the accretion-induced collapse of white dwarfs, *Mon. Not. Roy. Astron. Soc.* **525**, 6359 (2023), [arXiv:2306.04711 \[astro-ph.HE\]](#).
- [23] H. Dimmelmeier, C. D. Ott, A. Marek, and H. T. Janka, The Gravitational Wave Burst Signal from Core Collapse of Rotating Stars, *Phys. Rev. D* **78**, 064056 (2008), [arXiv:0806.4953 \[astro-ph\]](#).
- [24] A. J. Ruiter, L. Ferrario, K. Belczynski, I. R. Seitenzahl, R. M. Crocker, and A. I. Karakas, On the formation of neutron stars via accretion-induced collapse in binaries, *Mon. Not. Roy. Astron. Soc.* **484**, 698 (2019), [arXiv:1802.02437 \[astro-ph.SR\]](#).
- [25] P. Amaro-Seoane, J. Andrews, M. Arca Sedda, A. Askar, Q. Baghi, R. Balasov, I. Bartos, S. S. Bavera, J. Bellovary, C. P. Berry, *et al.*, Astrophysics with the laser interferometer space antenna, *Living Reviews in Relativity* **26**, 2 (2023).
- [26] E. Waxman, On the origin of fast radio bursts (FRBs), *Astrophys. J.* **842**, 34 (2017), [arXiv:1703.06723 \[astro-ph.HE\]](#).
- [27] B. Margalit, E. Berger, and B. D. Metzger, Fast Radio Bursts from Magnetars Born in Binary Neutron Star Mergers and Accretion Induced Collapse [10.3847/1538-4357/ab4c31](#) (2019), [arXiv:1907.00016 \[astro-ph.HE\]](#).
- [28] N. K. Largani, T. Fischer, and N. U. F. Bastian, Constraining the Onset Density for the QCD Phase Transition with the Neutrino Signal from Core-collapse Supernovae, *Astrophys. J.* **964**, 143 (2024), [arXiv:2304.12316 \[astro-ph.HE\]](#).
- [29] I. Sagert, T. Fischer, M. Hempel, G. Pagliara, J. Schaffner-Bielich, A. Mezzacappa, F. K. Thielemann, and M. Liebendorfer, Signals of the QCD phase transition in core-collapse supernovae, *Phys. Rev. Lett.* **102**, 081101 (2009), [arXiv:0809.4225 \[astro-ph\]](#).
- [30] S. Zha, E. P. O'Connor, M.-C. Chu, L.-M. Lin, and S. M. Couch, Gravitational-Wave Signature of a First-Order Quantum Chromodynamics Phase Transition in Core-Collapse Supernovae, *Phys. Rev. Lett.* **125**, 051102 (2020), [Erratum: *Phys. Rev. Lett.* 127, 219901 (2021)], [arXiv:2007.04716 \[astro-ph.HE\]](#).
- [31] T. Kuroda, T. Fischer, T. Takiwaki, and K. Kotake, Core-collapse Supernova Simulations and the Formation of Neutron Stars, Hybrid Stars, and Black Holes, *Astrophys. J.* **924**, 38 (2022), [arXiv:2109.01508 \[astro-ph.HE\]](#).
- [32] T. Fischer, QCD phase transition drives supernova explosion of a very massive star: Dependence on metallicity of the progenitor star, *Eur. Phys. J. A* **57**, 270 (2021), [arXiv:2108.00196 \[astro-ph.HE\]](#).
- [33] S. Zha, E. P. O'Connor, and A. da Silva Schneider, Progenitor Dependence of Hadron-quark Phase Transition in Failing Core-collapse Supernovae, *Astrophys. J.* **911**, 74 (2021), [arXiv:2103.02268 \[astro-ph.HE\]](#).
- [34] P. Jakobus, B. Mueller, A. Heger, A. Motornenko, J. Steinheimer, and H. Stoecker, The role of the hadron-quark phase transition in core-collapse supernovae, *Mon. Not. Roy. Astron. Soc.* **516**, 2554 (2022), [arXiv:2204.10397 \[astro-ph.HE\]](#).
- [35] E. R. Most, L. J. Papenfort, V. Dexheimer, M. Hanauske, S. Schramm, H. Stöcker, and L. Rezzolla, Signatures of quark-hadron phase transitions in general-relativistic neutron-star mergers, *Phys. Rev. Lett.* **122**, 061101 (2019), [arXiv:1807.03684 \[astro-ph.HE\]](#).
- [36] L. R. Weih, M. Hanauske, and L. Rezzolla, Postmerger Gravitational-Wave Signatures of Phase Transitions in Binary Mergers, *Phys. Rev. Lett.* **124**, 171103 (2020), [arXiv:1912.09340 \[gr-qc\]](#).
- [37] A. Prakash, D. Radice, D. Logoteta, A. Perego, V. Nedora, I. Bombaci, R. Kashyap, S. Bernuzzi, and A. Endrizzi, Signatures of deconfined quark phases in binary neutron star mergers, *Phys. Rev. D* **104**, 083029 (2021), [arXiv:2106.07885 \[astro-ph.HE\]](#).
- [38] S. Tootle, C. Ecker, K. Topolski, T. Demircik, M. Järvinen, and L. Rezzolla, Quark formation and phenomenology in binary neutron-star mergers using V-QCD, *SciPost Phys.* **13**, 109 (2022), [arXiv:2205.05691 \[astro-ph.HE\]](#).
- [39] T. Fischer, N.-U. F. Bastian, M.-R. Wu, P. Baklanov, E. Sorokina, S. Blinnikov, S. Typel, T. Klähn, and D. B. Blaschke, Quark deconfinement as a supernova explosion engine for massive blue supergiant stars, *Nature Astron.* **2**, 980 (2018), [arXiv:1712.08788 \[astro-ph.HE\]](#).
- [40] N. K. Largani, T. Fischer, S. Shibagaki, P. Cerdá-Durán, and A. Torres-Forné, Neutron stars in accreting systems – signatures of the QCD phase transition [10.1051/0004-6361/202348742](#) (2023), [arXiv:2311.15992 \[astro-ph.HE\]](#).
- [41] M. Naseri, G. Bozzola, and V. Paschalidis, Exploring pathways to forming twin stars, *Phys. Rev. D* **110**, 044037 (2024), [arXiv:2406.15544 \[astro-ph.HE\]](#).
- [42] L.-M. Lin, K. S. Cheng, M. C. Chu, and W. M. Suen, Gravitational waves from phase-transition induced collapse of neutron stars, *Astrophys. J.* **639**, 382 (2006), [arXiv:astro-ph/0509447](#).
- [43] E. B. Abdikamalov, H. Dimmelmeier, L. Rezzolla, and J. C. Miller, Relativistic simulations of the phase-transition-induced collapse of neutron stars, *Mon. Not. Roy. Astron. Soc.* **394**, 52 (2009), [arXiv:0806.1700 \[astro-ph\]](#).
- [44] A. K. L. Yip, P. C.-K. Cheong, and T. G. F. Li, Gravitational wave signatures from the phase-transition-induced collapse of a magnetized neutron star, (2023), [arXiv:2305.15181 \[astro-ph.HE\]](#).
- [45] N.-U. F. Bastian, Phenomenological quark-hadron equations of state with first-order phase transitions for astrophysical applications, *Phys. Rev. D* **103**, 023001 (2021), [arXiv:2009.10846 \[nucl-th\]](#).
- [46] J. Antoniadis *et al.*, A Massive Pulsar in a Compact Relativistic Binary, *Science* **340**, 6131 (2013), [arXiv:1304.6875 \[astro-ph.HE\]](#).
- [47] E. Fonseca *et al.*, Refined Mass and Geometric Measurements of the High-mass PSR J0740+6620, *Astrophys. J. Lett.* **915**, L12 (2021), [arXiv:2104.00880 \[astro-ph.HE\]](#).
- [48] S. Blacker, N.-U. F. Bastian, A. Bauswein, D. B. Blaschke, T. Fischer, M. Oertel, T. Sultanis, and S. Typel, Constraining the onset density of the hadron-quark phase transition with gravitational-wave observations, *Phys. Rev. D* **102**, 123023 (2020), [arXiv:2006.03789 \[astro-ph.HE\]](#).
- [49] N. Stergioulas and J. L. Friedman, Comparing models of rapidly rotating relativistic stars constructed by two numerical methods, *Astrophys. J.* **444**, 306 (1995), [arXiv:astro-ph/9411032](#).
- [50] P. C.-K. Cheong, L.-M. Lin, and T. G.-F. Li, Gmnu: Toward multigrad based Einstein field equations solver for general-relativistic hydrodynamics simulations [10.1088/1361-6382/ab8e9c](#) (2020), [arXiv:2001.05723 \[gr-](#)

- qc].
- [51] P. C.-K. Cheong, A. T.-L. Lam, H. H.-Y. Ng, and T. G. F. Li, Gmnu: paralleled, grid-adaptive, general-relativistic magnetohydrodynamics in curvilinear geometries in dynamical space-times, *Mon. Not. Roy. Astron. Soc.* **508**, 2279 (2021), [arXiv:2012.07322 \[astro-ph.IM\]](#).
- [52] P. C.-K. Cheong, D. Y. T. Pong, A. K. L. Yip, and T. G. F. Li, An Extension of Gmnu: General-relativistic Resistive Magnetohydrodynamics Based on Staggered-meshed Constrained Transport with Elliptic Cleaning, *Astrophys. J. Suppl.* **261**, 10.3847/1538-4365/ac6cec (2022).
- [53] P. C.-K. Cheong, H. H.-Y. Ng, A. T.-L. Lam, and T. G. F. Li, General-relativistic Radiation Transport Scheme in Gmnu. I. Implementation of Two-moment-based Multi-frequency Radiative Transfer and Code Tests, *Astrophys. J. Suppl.* **267**, 38 (2023), [arXiv:2303.03261 \[astro-ph.IM\]](#).
- [54] H. H.-Y. Ng, P. C.-K. Cheong, A. T.-L. Lam, and T. G. F. Li, General-relativistic Radiation Transport Scheme in Gmnu. II. Implementation of Novel Microphysical Library for Neutrino Radiation—Weakhub, *Astrophys. J. Suppl.* **272**, 9 (2024), [arXiv:2309.03526 \[astro-ph.HE\]](#).
- [55] I. Cordero-Carrion, P. Cerda-Duran, H. Dimmelmeier, J. L. Jaramillo, J. Novak, and E.ourgoulhon, An Improved constrained scheme for the Einstein equations: An Approach to the uniqueness issue, *Phys. Rev. D* **79**, 024017 (2009), [arXiv:0809.2325 \[gr-qc\]](#).
- [56] H. H.-Y. Ng, J.-L. Jiang, C. Musolino, C. Ecker, S. D. Tootle, and L. Rezzolla, Hybrid approach to long-term binary neutron-star simulations, *Phys. Rev. D* **109**, 064061 (2024), [arXiv:2312.11358 \[gr-qc\]](#).
- [57] J.-L. Jiang, H. H.-Y. Ng, M. Chabanov, and L. Rezzolla, Long-term impact of the magnetic-field strength on the evolution and electromagnetic emission by neutron-star merger remnants, (2025), [arXiv:2502.14962 \[astro-ph.HE\]](#).
- [58] D. Radice, S. Bernuzzi, A. Perego, and R. Haas, A new moment-based general-relativistic neutrino-radiation transport code: Methods and first applications to neutron star mergers, *MNRAS* **512**, 1499 (2022), [arXiv:2111.14858 \[astro-ph.HE\]](#).
- [59] P. C.-K. Cheong, F. Foucart, M. D. Duez, A. Offermans, N. Muhammed, and P. Chawhan, Energy-dependent and Energy-integrated Two-moment General-relativistic Neutrino Transport Simulations of a Hypermassive Neutron Star, *Astrophys. J.* **975**, 116 (2024), [arXiv:2407.16017 \[astro-ph.HE\]](#).
- [60] L. Pareschi and G. Russo, Implicit–explicit runge–kutta schemes and applications to hyperbolic systems with relaxation, *Journal of Scientific computing* **25**, 129 (2005).
- [61] H. Nagakura, S. Furusawa, H. Togashi, S. Richers, K. Sumiyoshi, and S. Yamada, Comparing treatments of weak reactions with nuclei in simulations of core-collapse supernovae, *Astrophys. J. Suppl.* **240**, 38 (2019), [arXiv:1812.09811 \[astro-ph.HE\]](#).
- [62] M. Liebendoerfer, A Simple parameterization of the consequences of deleptonization for simulations of stellar core collapse, *Astrophys. J.* **633**, 1042 (2005), [arXiv:astro-ph/0504072](#).
- [63] Z. Lin, S. Zha, E. P. O’Connor, and A. W. Steiner, Detectability of neutrino-signal fluctuations induced by the hadron-quark phase transition in failing core-collapse supernovae, *Phys. Rev. D* **109**, 023005 (2024), [arXiv:2203.05141 \[astro-ph.HE\]](#).
- [64] G. Ricciardi, N. Vignaroli, and F. Vissani, An accurate evaluation of electron (anti-)neutrino scattering on nucleons, *JHEP* **08**, 212, [arXiv:2206.05567 \[hep-ph\]](#).
- [65] A. Strumia and F. Vissani, Precise quasielastic neutrino/nucleon cross-section, *Phys. Lett. B* **564**, 42 (2003), [arXiv:astro-ph/0302055](#).
- [66] M. Ikeda *et al.* (Super-Kamiokande), Search for Supernova Neutrino Bursts at Super-Kamiokande, *Astrophys. J.* **669**, 519 (2007), [arXiv:0706.2283 \[astro-ph\]](#).
- [67] K. Abe *et al.* (Hyper-Kamiokande), Hyper-Kamiokande Design Report, (2018), [arXiv:1805.04163 \[physics.ins-det\]](#).
- [68] S. Cheng, J. D. Cummings, B. Ménard, and S. Toonen, Double white dwarf merger products among high-mass white dwarfs, *The Astrophysical Journal* **891**, 160 (2020).
- [69] S. E. Woosley, A. Heger, and T. A. Weaver, The evolution and explosion of massive stars, *Rev. Mod. Phys.* **74**, 1015 (2002).
- [70] T. Fischer, M.-R. Wu, B. Wehmeyer, N.-U. F. Bastian, G. Martínez-Pinedo, and F.-K. Thielemann, Core-collapse Supernova Explosions Driven by the Hadron-quark Phase Transition as a Rare r -process Site, *Astrophys. J.* **894**, 9 (2020), [arXiv:2003.00972 \[astro-ph.HE\]](#).
- [71] G. Guo, G. Martínez-Pinedo, A. Lohs, and T. Fischer, Charged-Current Muonic Reactions in Core-Collapse Supernovae, *Phys. Rev. D* **102**, 023037 (2020), [arXiv:2006.12051 \[hep-ph\]](#).
- [72] P. C.-K. Cheong, F. Foucart, H. H.-Y. Ng, A. Offermans, M. D. Duez, N. Muhammed, and P. Chawhan, Influence of neutrino-electron scattering and neutrino-pair annihilation on hypermassive neutron star, (2024), [arXiv:2410.20681 \[astro-ph.HE\]](#).
- [73] H. H.-Y. Ng, C. Musolino, S. D. Tootle, and L. Rezzolla, Accurate muonic interactions in neutron-star mergers and impact on heavy-element nucleosynthesis, (2024), [arXiv:2411.19178 \[astro-ph.HE\]](#).

END MATTER

Hydrodynamical profile comparison of PNS and PHS.

The first-order QCD PT triggers a second collapse, causing rapid latent heat absorption and a shock that reshapes the PHS hydrodynamics. Figure 5 shows the radial hydrodynamical profiles at 50 ms before and after t_Q for RDF-1.5 model. The vertical dashed lines indicate the radii of PNS (red) and PHS (blue), respectively. Note that by $t - t_Q = 50$ ms, the PHS attains a quasi-steady state and is much more compact (see also Fig. 1).

The PHS exhibits a cooler core compared to the PNS at $t - t_Q = -50$ ms, as the thermal energy is converted to latent heat during the formation of deconfined quark matter. In contrast, the shocked envelope outside the PHS (for $r > 20$ km) is slightly hotter.

Unlike the PNS at $t - t_Q = -50$ ms, which features oscillating matter in its envelope, the quasi-steady PHS continues to ejects materials with $v^r > 0$ as long as 300 ms. In these outer layers, the velocity can exceed $0.1 c$ at $r > 100$ km. This outflow is driven by the heavily perturbed PHS, where neutrino interactions become active again in the shocked regions. These neutrinos deposit energy via reabsorption in the outer layers, leading to the ejection of about 0.1% of the PHS mass by $t - t_Q = 300$ ms.

The fractions of deconfined quark matter, mixed-phase matter and hadronic matter in the PHS are highly non-linear and depend on the EOS properties that determine the collapse dynamics and the strength of the second bounce (the properties of PHS can be found in the right columns of Table II). In all models, the mixed-phase mantle is sandwiched between the hadronic envelope and deconfined-quark core with a small size of at most 2 km due to its softness among all cases. Even a special case of RDF-1.1, where the mass of mixed-phase mantle exceeds that of quark core, follows this pattern.

Particular attention should be paid to this special case of RDF-1.1. Its PNS collapse driven by the PT is weaker and slower due to its high $\rho_{\text{mixed,c}}$, leading to a longer timescale of cooling and lower velocities of collapsing matter before t_Q , and a small decrease in both $Y_{q,c}$ and ρ_c at $t - t_Q \approx -3.8$ ms shown in Fig. 1. These result in a much lighter quark core surrounded by a significantly more mixed-phase mantle. The result of RDF-1.1 case is nearly a critical case where the progenitor mass with $1.51 M_\odot$ (gravitational mass) is close to the onset mass of the EOS with $1.57 M_\odot$ shown in Table I, and it is also the reason of oscillating in $Y_{q,c}$ after second bounce.

Two additional robust features appear in all models. First, a cavity with a low proton fraction ($Y_p \sim 0.1$) forms at about $t - t_b \sim 10$ ms, coinciding with the ν_e burst shortly after core bounce, and this cavity persists until the PHS forms (see the Y_p profile in Fig. 5). The

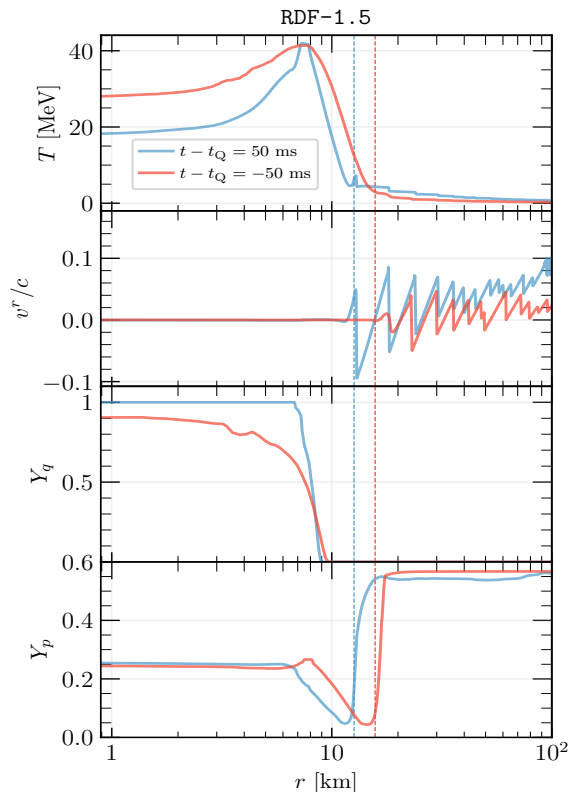


FIG. 5. Radial snapshots of temperature T , radial velocity v^r/c , proton fraction Y_p , and quark fraction Y_q of RDF-1.5 model at 50 ms before (red) and 50 ms after (blue) the time moment of t_Q . Dashed lines correspond to the density at $\rho = 10^{11} \text{ g cm}^{-3}$.

second shock, originating from the deconfined quark core beneath the cavity, passes through this low Y_p region, emitting primarily $\bar{\nu}_e$ via positron (e^+) capture. Consequently, the second burst is predominantly composed of $\bar{\nu}_e$ for all EOSs, similar to the behavior reported in CCSN simulations with a QCD PT [28, 39]. In contrast, the first neutrino burst, which results from the first bounce, is dominated by ν_e emission due to the proton-rich environment of the newly formed PNS.

Finally, the high temperature of the PHS lead to a greater integrated emission of ν_x compared to ν_e during the second burst. Furthermore, the second burst generally produces neutrinos with higher average energy across all species compared to the first burst, consistent with findings of Ref. [28].

Comparison of neutrino bursts luminosity.

Electron captures prior to core bounce steadily increase \mathcal{L}_{ν_e} . The collapse halts due to hadronic matter stiffening, triggering an outward shock that dissociates heavy nuclei, enhancing ν_e production via e^- captures. This results in a luminous ν_e burst from proton captures in shock-heated matter, peaking at $t = t_b$ in Fig. 6. Compression and Doppler redshifting cause a dip in \mathcal{L}_{ν_e}

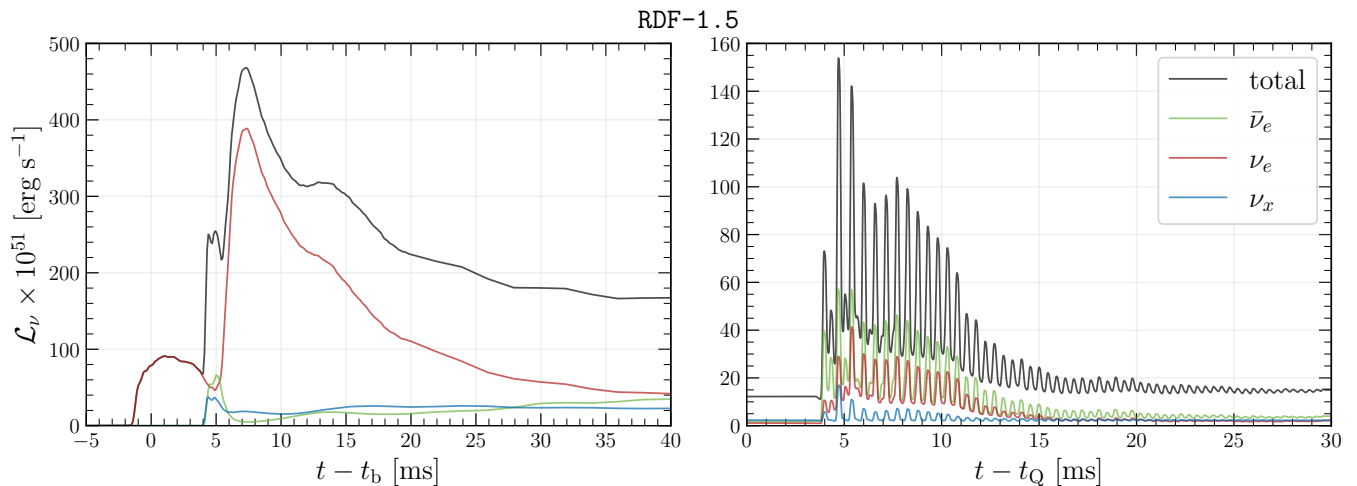


FIG. 6. Neutrino luminosity \mathcal{L}_ν of the first and the second burst in model with RDF-1.5 for total luminosity (black), \mathcal{L}_{ν_e} (red), $\mathcal{L}_{\bar{\nu}_e}$ (green) and \mathcal{L}_{ν_x} (blue), respectively.

around 4 ms later.

As the shock breaks out, \mathcal{L}_{tot} peaks at 4.6×10^{53} ergs⁻¹, with \mathcal{L}_{ν_e} peaks at 3.8×10^{53} ergs⁻¹, while shock-heated matter enhances pair processes, leading to $\bar{\nu}_e$ and ν_x peaks at 4×10^{52} ergs⁻¹ and 6×10^{52} ergs⁻¹, respectively. Given the similarity of hadronic matter modelling near nuclear saturation density across RDF EOS models, this first neutrino burst behavior is generic.

In contrast, the second neutrino burst differs significantly due to a different emission mechanism. The stiffening of deconfined quark matter halts the PT-induced collapse, generating a second shock. The low-proton-fraction cavity facilitates e^+ capture, leading to a $\bar{\nu}_e$ -dominated burst. Unlike the first burst, all species reach a local maximum in Fig. 6. \mathcal{L}_{tot} peaks at 1.6×10^{53} ergs⁻¹ with \mathcal{L}_{ν_e} , $\mathcal{L}_{\bar{\nu}_e}$ and \mathcal{L}_{ν_x} peak at 6×10^{52} ergs⁻¹, 4×10^{52} ergs⁻¹, 2×10^{52} ergs⁻¹ respectively. Multiple follow-up shocks from PHS oscillations introduce an oscillatory pattern.

The relative luminosities of the first and second bursts depend on EOS properties, particularly the onset density, which affects the shock strength. (See discussion of Fig. 4). Consequently, the total luminosity of model with RDF-1.9 and RDF-1.2 are larger than the first neutrino burst, with $\mathcal{L}_{\text{tot}} = 2.99 \times 10^{54}$ ergs⁻¹ and 1.35×10^{54} ergs⁻¹ respectively. On the other hand, \mathcal{L}_{tot} of the second neutrino burst in RDF-1.5 and RDF-1.1 models are weaker than the first, with $\mathcal{L}_{\text{tot}} = 2 \times 10^{53}$ ergs⁻¹ and 5.47×10^{52} ergs⁻¹ respectively. Thus, no clear correlations exist between the total luminosities of the first and second bursts, as these are highly sensitive to EOS.